# SUPPLEMENTARY FIGURES

**Supplementary Figure. 1| Fragment size distribution and M-bias plot of cfDNA WGBS data.**

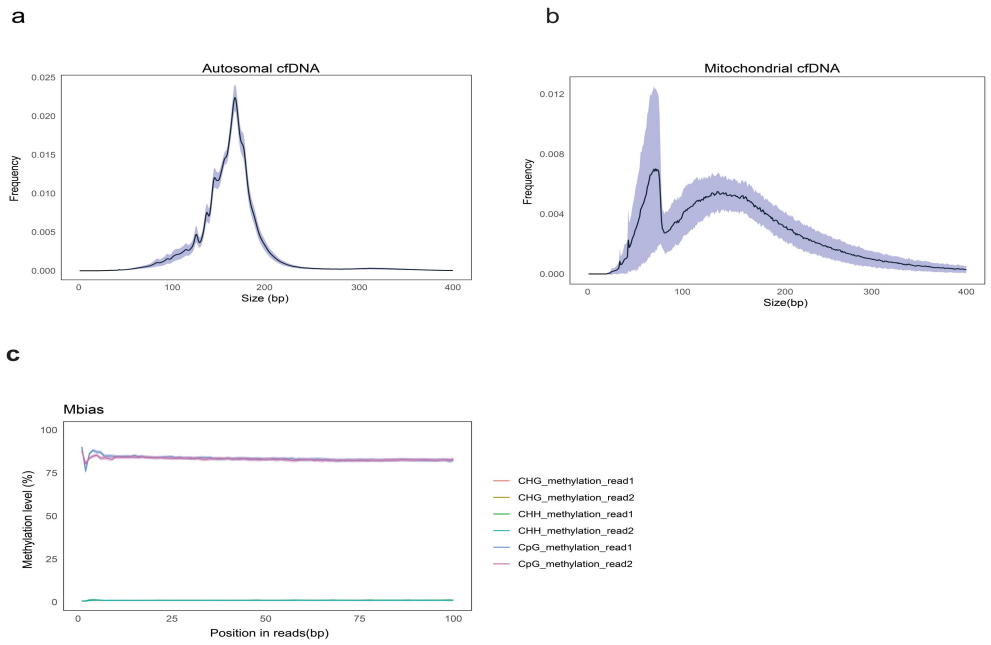


(a-b) Fragment size distribution of autosomal and mitochondrial cfDNA. The black lines represent the mean frequency of each insert size, while the shaded regions represent the mean ± SD. (c). Methylation bias (M-bias) across read positions.

**Supplementary Figure. 2 | Distribution of age-associated CpGs on autosomes and GO enrichment analysis of age-associated genes**

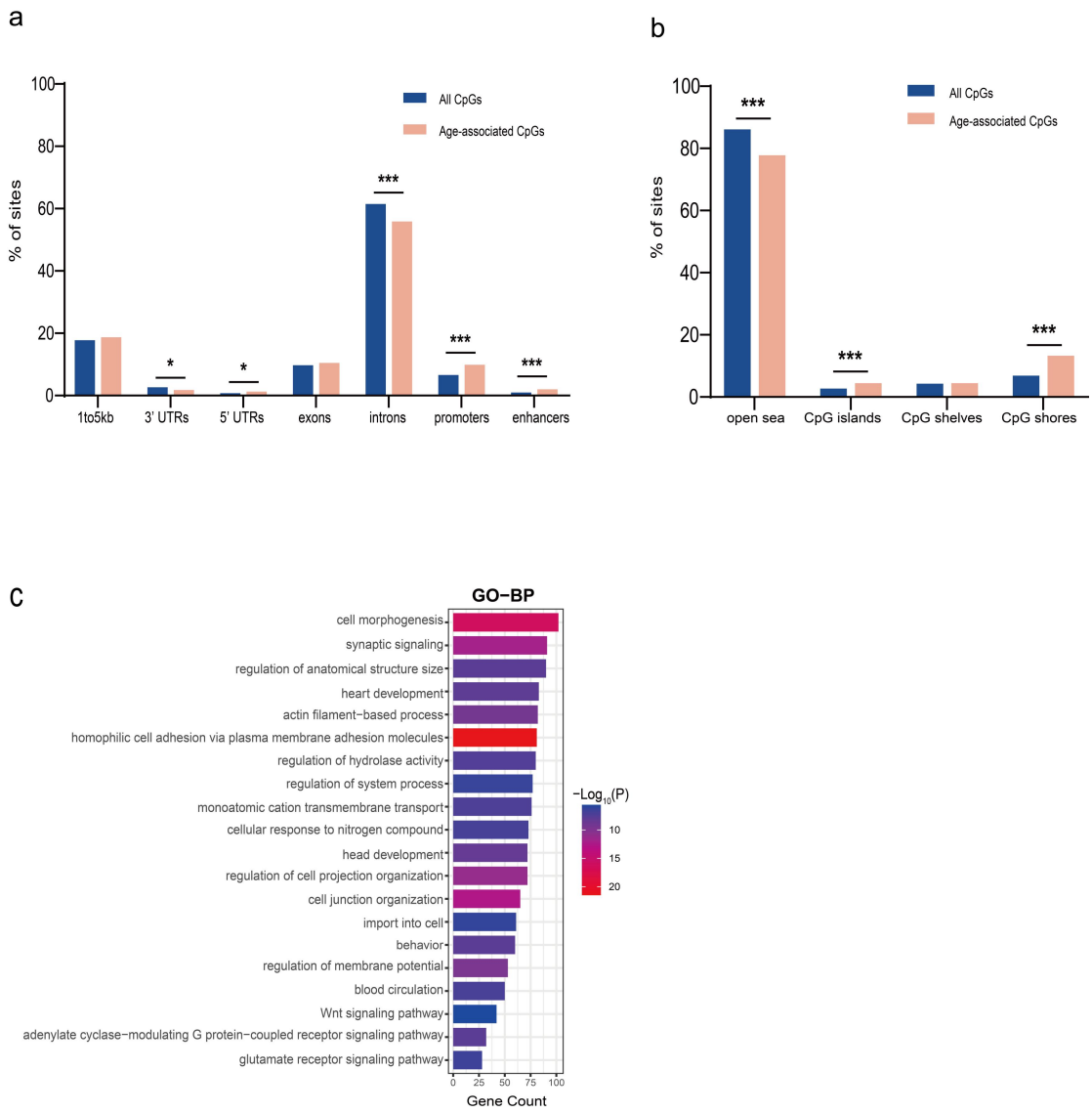


(a-b) Distribution of age-associated CpGs in gene regions(a) and CpG regions(b). The significance was calculated using the chi-square test and corrected with Bonferroni correction, *Padj<0.05, **Padj<0.01, and ***Padj<0.001. (c) GO enrichment analysis of 1,587 genes.

**Supplementary Figure. 3 | Validation of the cfDNA methylation clock using the cfDNA WGBS data of 23 healthy individuals (GSE186458).**

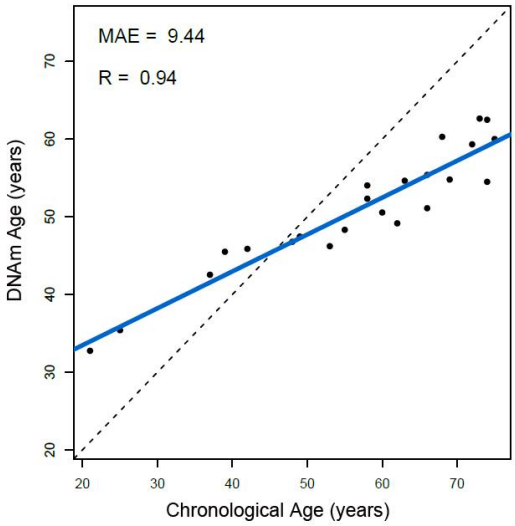


The plot shows the relationship between chronological age and epigenetic age. The blue line is the regression line of epigenetic age on chronological age. Pearson's correlation coefficients (r) and median absolute error (MAE) are denoted.

**Supplementary Figure. 4 | Methylation rates of seven CpGs associated with age and sex.** All CpGs were annotated to the *FIGN* gene, except for chr6:13559260, which was not annotated to any gene.

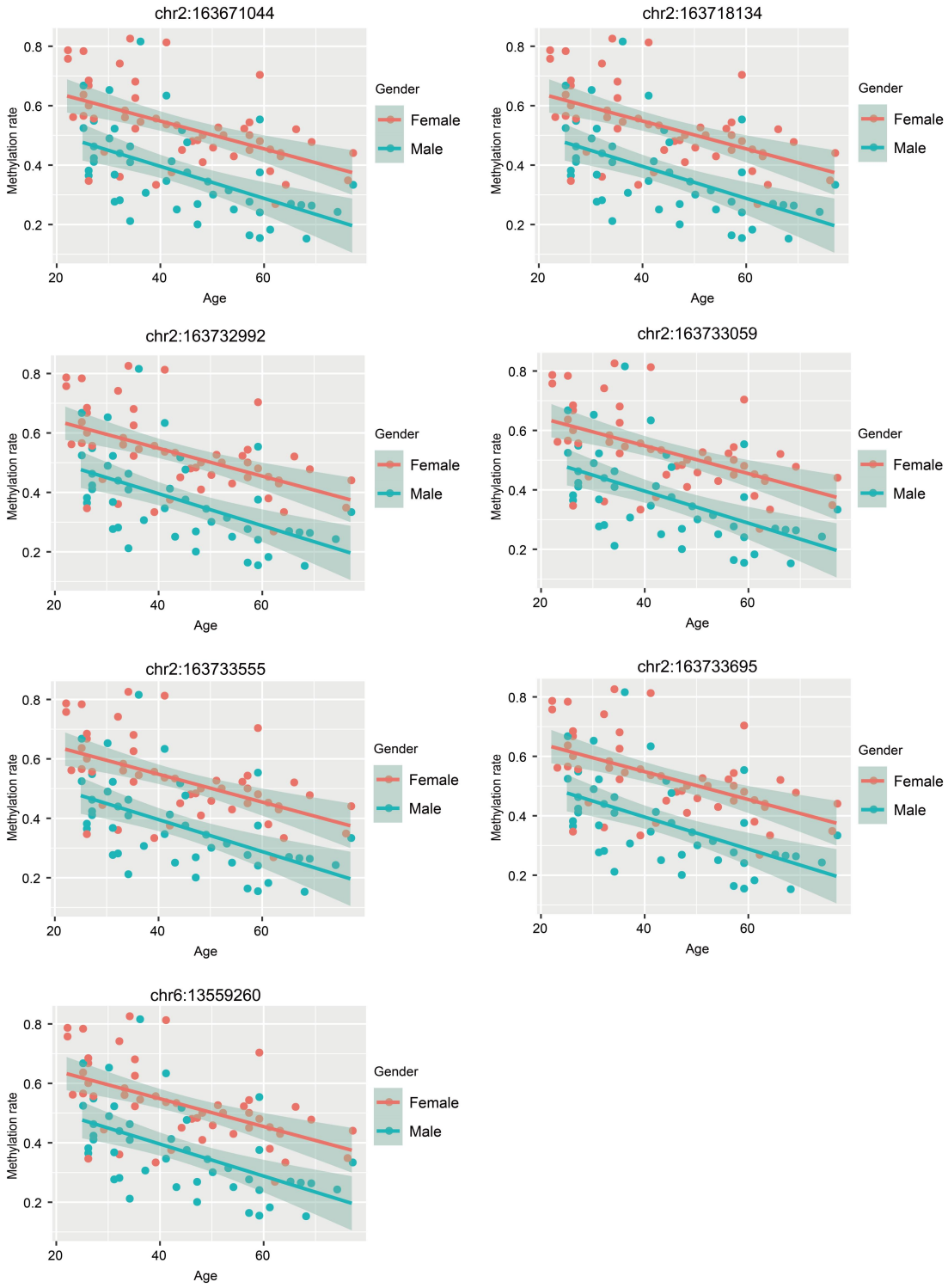

**Supplementary Figure. 5 | Distribution of sex-associated CpGs on autosomes.**

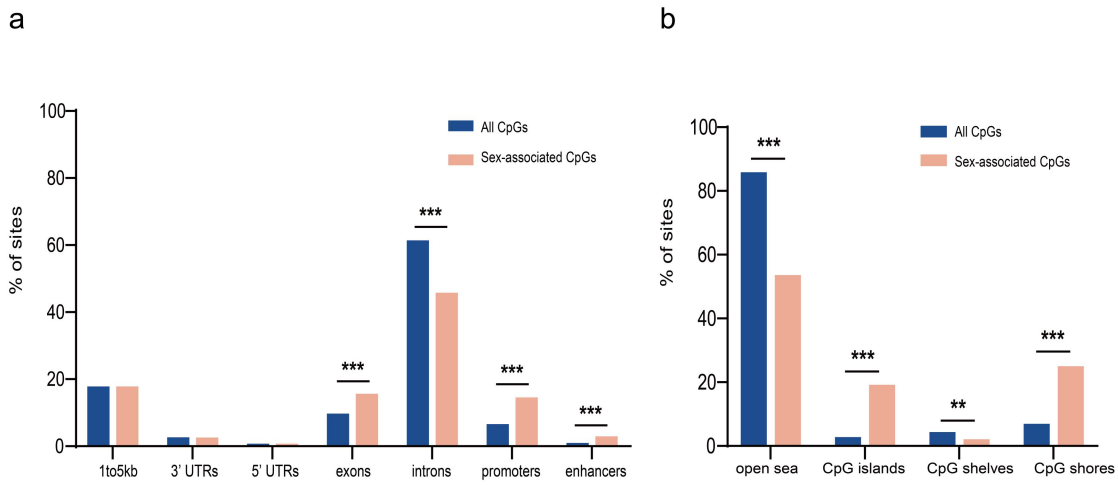


(a-b) Distribution of sex-associated CpGs in gene regions(a) and CpG regions(b). The significance was calculated using the chi-square test and corrected with Bonferroni correction, *Padj<0.05, **Padj<0.01, and ***Padj<0.001.

**Supplementary Figure. 6 | Tissue-specific gene enrichment analysis for the 324 genes containing sex-associated CpGs.**

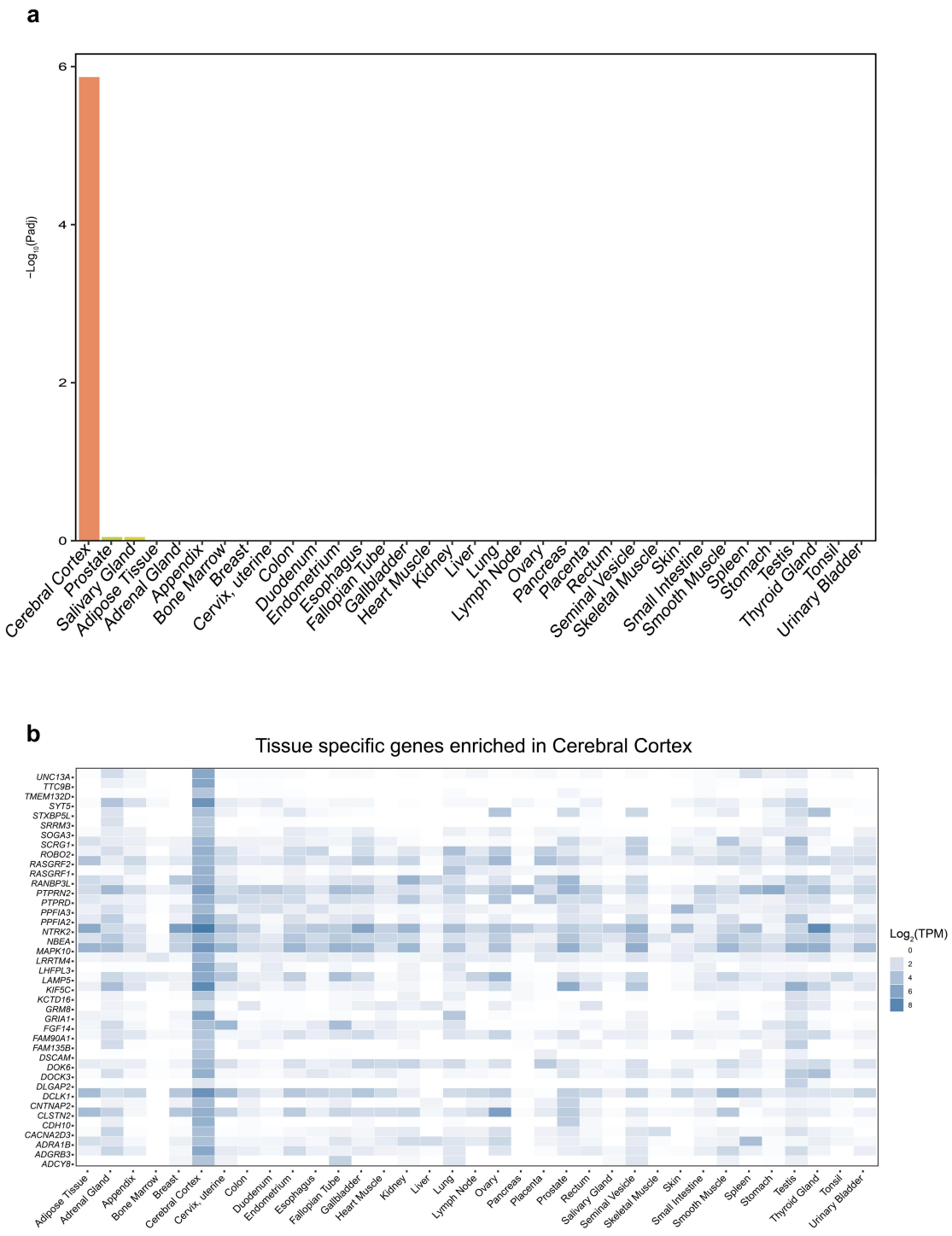


(a) Tissue-specific gene enrichment of the 324 genes in 35 tissues. (b) Tissue-specific genes in the cerebral cortex.

**Supplementary Figure. 7 | UpSet plot showing the intersects of the genes with five DNA methylation patterns on the X chromosome (pattern A, B, C, D, and other)**

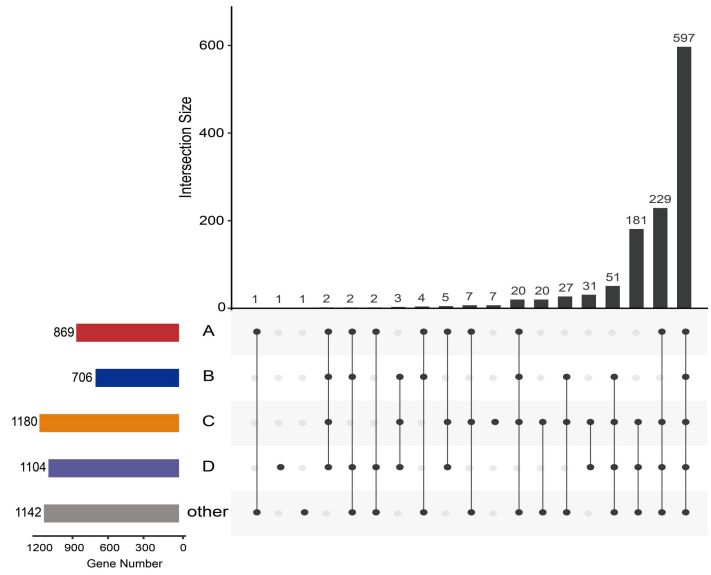

**Supplementary Figure. 8 | Cell-type of origin analysis of the cfDNA for 98 participants based on the methylation profile** (Deconvolution method: Moss et al. [17].)

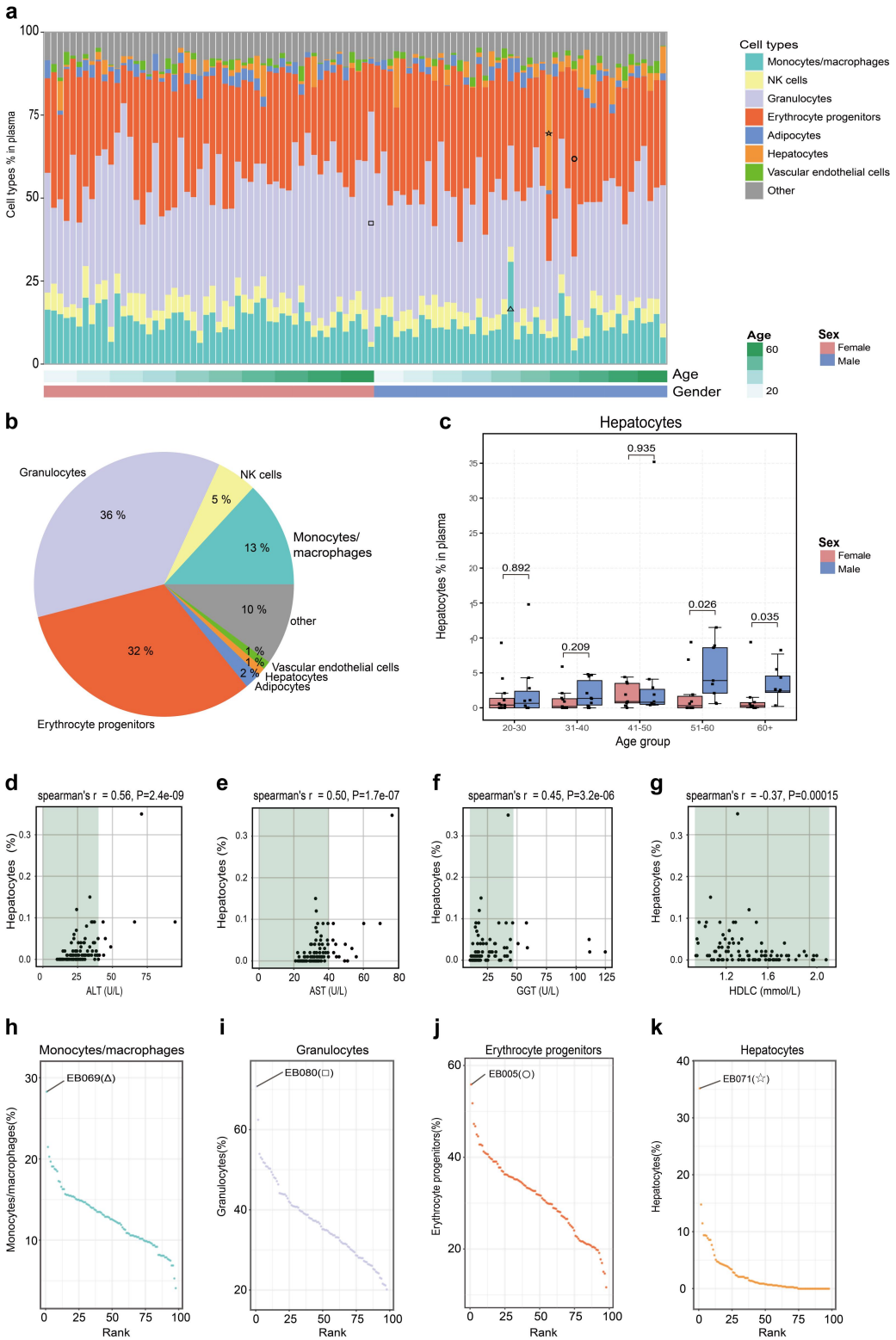

(a) Cell-type composition of plasma cfDNA for each individual (n=98). (b) Cellular contributors to cfDNA (median value of 98 samples). (c) Boxplot of the hepatocytes-derived cfDNA proportions of females (rose red) and males (blue) in different age groups. Box plots show median ± interquartile range (IQR) and 1.5 IQR ranges (whiskers). The significant p values were calculated by the Wilcoxon rank-sum test. (d-g) Spearman's correlation between the hepatocytes-derived cfDNA proportion and ALT, AST, GGT, and HDLC, respectively. (h-k) The rank of samples based on cfDNA derived from monocytes/macrophages, granulocytes, erythroid progenitor cells, and hepatocytes. Special symbols triangle (Δ), square (□), hollow circle (○), and star (☆) in (a) represent the corresponding participants in (h-k).

**Supplementary Figure. 9 | The proportion of granulocytes-derived cfDNA increases with age in females**

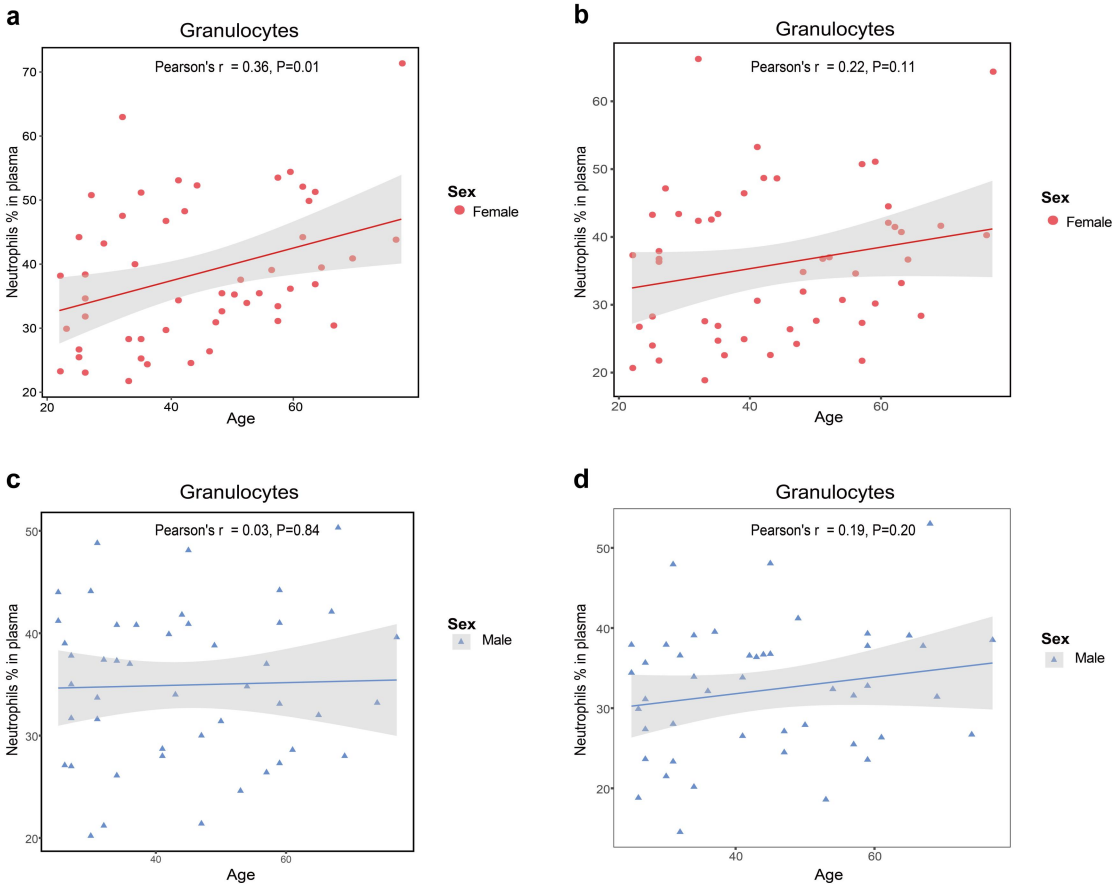


Deconvolution results of granulocytes using two methods developed by (a)(c) Moss et al. [17] and (b)(d) Loyfer et al. [18].

**Supplementary Figure. 10 | The proportion of monocytes-derived cfDNA decreases with age in females but not in males.** (Deconvolution method: Moss et al. [17].)

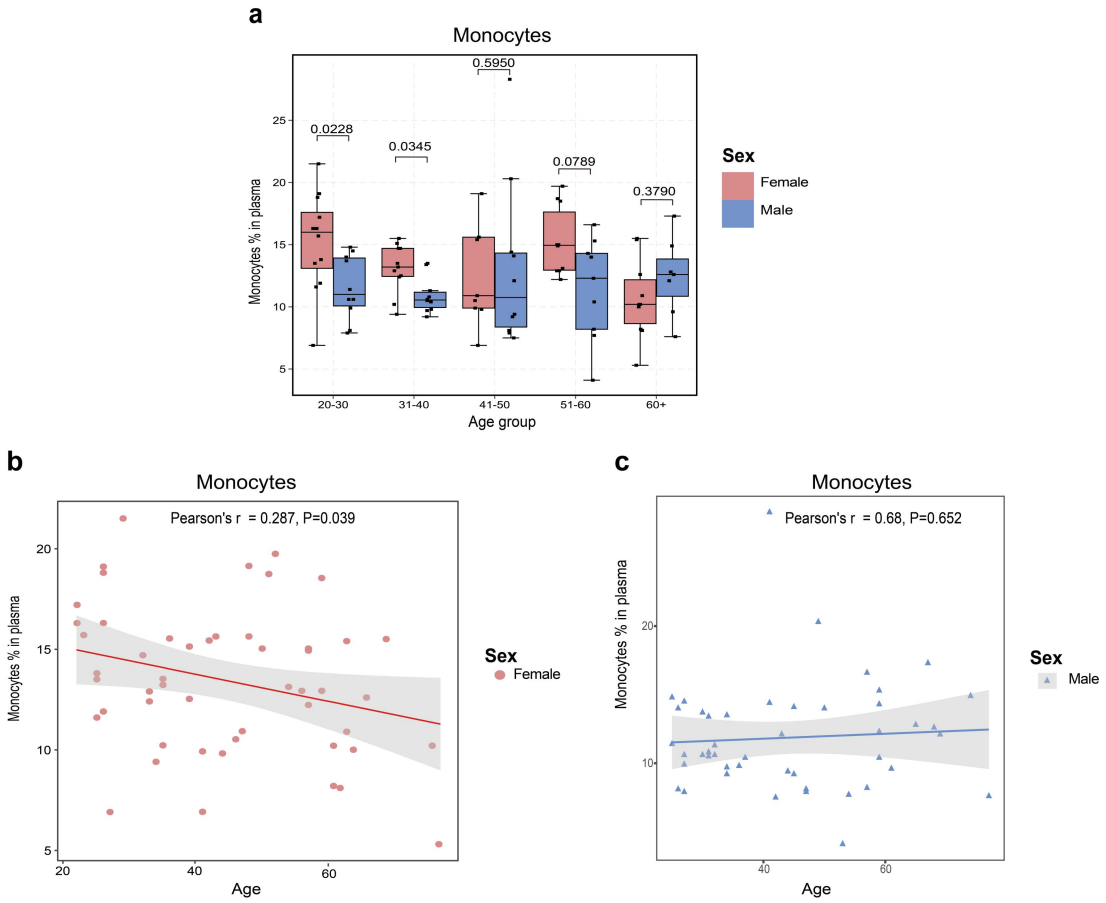


(a) Boxplot comparing the monocyte-derived cfDNA proportions in females (rose red) and males (blue) across age groups. (b) Monocyte-derived cfDNA decreases significantly with age in females. (c) Monocyte-derived cfDNA remains unchanged in males.